THE JOURNAL OF PHYSICAL CHEMISTRY C
A JOURNAL OF THE AMERICAN CHEMICAL SOCIETY

pubs.acs.org/JPCC
Article

Deep Learning Methods for Colloidal Silver Nanoparticle Concentration and Size Distribution Determination from UV−Vis Extinction Spectra

Tomas Klinavičius,* Nadzeya Khinevich, Asta Tamulevičienė, Loïc Vidal, Sigitas Tamulevičius, and Tomas Tamulevičius*

Cite This: J. Phys. Chem. C 2024, 128, 9662−9675
Read Online

ACCESS | Metrics & More | Article Recommendations | Supporting Information

ABSTRACT: Electron microscopy, while reliable, is an expensive, slow, and inefficient technique for thorough size distribution characterization of both monodisperse and polydisperse colloidal nanoparticles. If rapid *in situ* characterization of colloid samples is to be achieved, a different approach, based on fast, widely accessible, and inexpensive optical measurements such as UV−vis spectroscopy in combination with spectral interpretation related to Mie scattering theory, is needed. In this article, we present a tandem deep neural network (DNN) for the size distribution and concentration prediction of close to spherical silver colloidal nanoparticle batches synthesized via the seeded-growth method. The first DNN identified the dipole component of the localized surface plasmon resonance, and the second one determined the size distribution from the isolated spectral component. The training data was engineered to be bias-free and generated numerically. High prediction accuracy with root-mean-square percentage error of mean size down to 1.2% was achieved, spanning the entire prediction range from 1 up to 150 nm in radius, suggesting the possible extension limits of the effective medium theory used for simulating the spectra. The DNN-predicted nanoparticle concentrations also were very close to the ones expected based on synthesis precursor contents as well as those measured by atomic absorption spectroscopy.

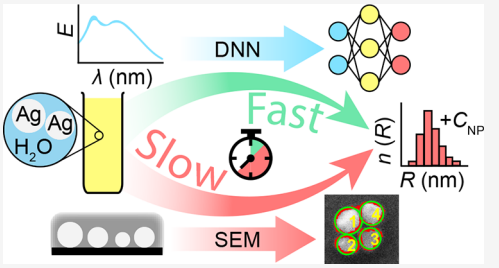

INTRODUCTION

Virtually any pure solid-state material, such as metals, semiconductors, ceramics, and others,[1] or its combination can exist in the nanoparticle (NP) form.[2] NP synthesis methods can be divided into two broad categories—physical and chemical methods.[3] Physical methods use physical interactions, such as mechanical[4] or thermal,[5] to produce NPs from the bulk material. Physical synthesis methods also include laser ablation of solids in a liquid[6] and sputtering.[7] On the other hand, chemical methods use chemical reactions, such as chemical reduction[8,9] or deposition on a surface from vapor.[10] Regardless of the synthesis method, NPs always have a certain size distribution, typically a log-normal one.[11,12]

Unlike microparticles, NPs exhibit size-dependent properties, which are different from those of their bulk counterparts.[13] Localized surface plasmon resonance (LSPR) is a plasmonic phenomenon[14] that can be optically excited in metallic and semiconductor NPs.[15] The LSPR is observed in the extinction ($E(\lambda)$) spectrum of the NPs where multiple peaks, which correspond to different resonance modes, can manifest.[16] As a phenomenon, LSPR is highly sensitive to the refractive index of the ambient medium, making it suitable for biomolecule[17] and virus[18] detection applications. This and other unique properties of NPs make them exceptionally useful in biomedicine for the detection of antigens,[19] biological warfare agents,[20] and gene delivery.[21] They also found environmental and energy-related applications for cleaning up pollutants in the water[22] and conversion of CO_2 to carbon-based fuels,[23] along with water splitting for the generation of green hydrogen[24] and enhancing solar energy harvesting.[25,26] The NP size distribution is one of the most critical parameters for their catalytic efficacy[27] as well as other cellular interactions,[28] especially in cancer detection,[29] and treatment[30] where knowing the NP size distribution is essential. Due to such wide application and the importance of size, simple yet rapid characterization approaches of the NP size distribution information are of special interest in an industrial setting.[31]

Estimating the characteristic size dimensions of NPs experimentally is generally a difficult and time-consuming task. One highly popular method is direct imaging of drop-casted NPs by scanning electron microscopy (SEM) or transmission electron microscopy (TEM),[32] as both methods measure the true geometric (Feret[33]) size of the NPs. Producing statistically reliable NP distributions by these methods requires multiple

Received: April 15, 2024
Revised: May 22, 2024
Accepted: May 24, 2024
Published: June 4, 2024

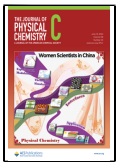

https://doi.org/10.1021/acs.jpcc.4c02459
J. Phys. Chem. C 2024, 128, 9662−9675

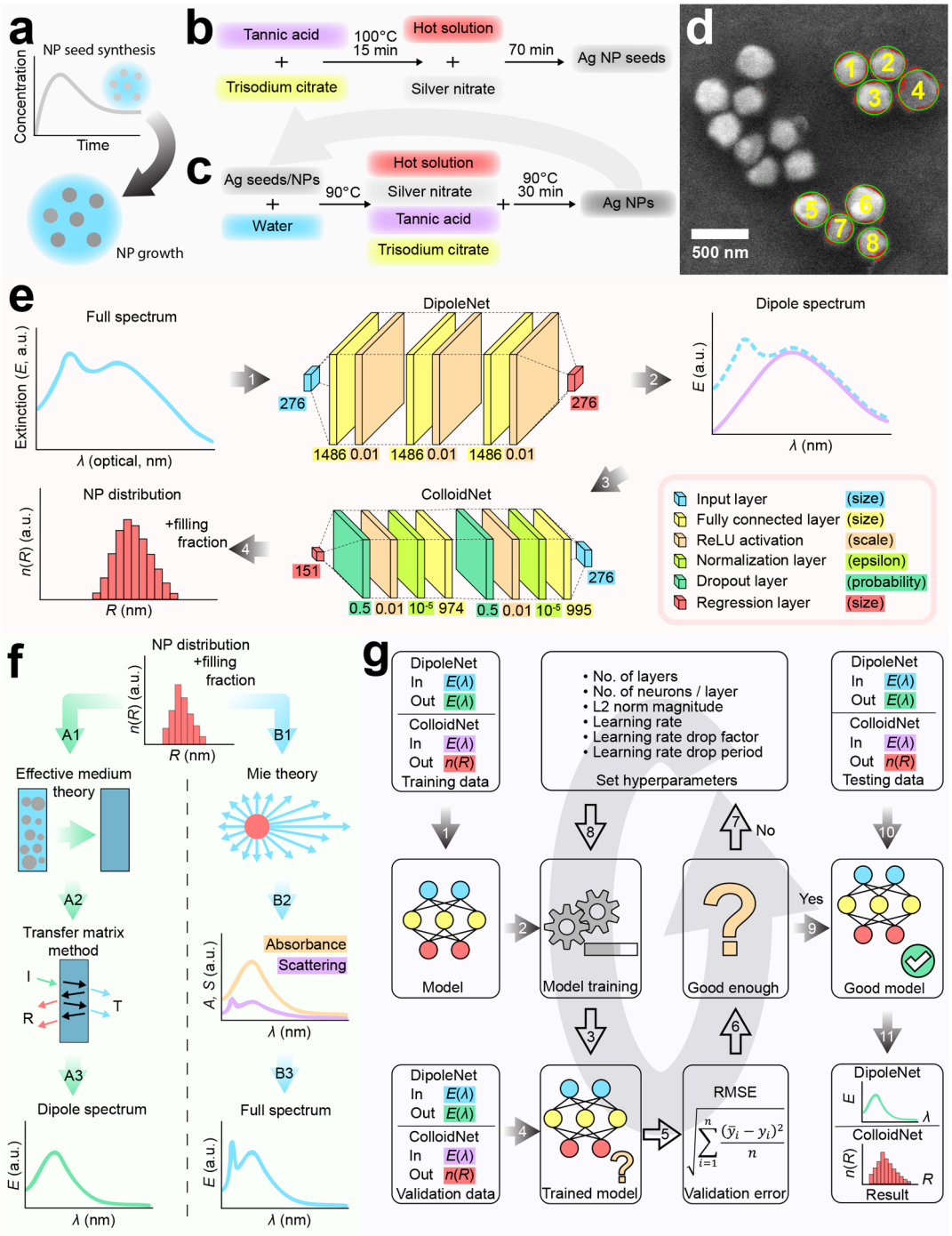

Figure 1. Experimental and computational methods used for Ag NP colloid $E(\lambda)$ spectral analysis for obtaining the effective NP radius size distribution ($n(R)$). (a) Graphical representation of Ag NP seed synthesis and subsequent growth. (b) Chemical reaction for the Ag NP seeds colloid synthesis. (c) Reaction for Ag NP synthesis. (d) Determination of the empirical NP effective radius distribution from SEM micrographs, and overlaid graphics indicates the automated area analysis results used for extraction of the effective radius distribution of numbered NPs. (e) Working principle of the proposed tandem DNN system for determining NP concentration and radius distribution in a colloidal solution from its $E(\lambda)$ spectra; the legend explains the layers and the parameters of the DNNs used where "DipoleNet" is responsible for subtracting the dipole peak and the "ColloidNet" for finding the radius distribution from the pretreated $E(\lambda)$ spectra, and arrows indicate the order of operations (input of extinction spectrum to DipoleNet—1, obtaining output from DipoleNet—"2", inputting output of DipoleNet to ColloidNet—"3" and obtaining output from ColloidNet—"4"). (f) Generation of training data for both DNNs using effective medium theory with TMM (computation of effective NP permittivity—"A1", input of effective medium to TMM—"A2", and computation using TMM—"A3") and Mie theory (computation of parameters for Mie theory using NP distribution—"B1" and performing computations of absorbance and scattering "B2" to obtain $E(\lambda)$ "B3"). (g) Workflow for hyperparameter optimization (HPO) and network testing for both networks (input of training data 1 to the model 2, training the model 3, inputing validation data to a trained model 4, obtaining validation error "5", comparing to a desired performance metric "6", setting different hyperparameters "7" if performance was not satisfactory and using new hyperparameters for training "8" or, if performance is satisfactory, obtaining a trained model "9", which is tested with testing data "10", to obtain outputs (size and concentration analysis results) "11").

https://doi.org/10.1021/acs.jpcc.4c02459
J. Phys. Chem. C 2024, 128, 9662−9675

micrographs of the NPs and automatic image processing.[34] Probe-based methods such as atomic force microscopy are also used to measure the size distribution of surface-deposited NPs, but the measured sizes are inherently nongeometric due to convolution between the probe tip and the NPs[35] and are not the true NP sizes. Other size measurement techniques are optical, such as dynamic light scattering (DLS).[36] DLS is used for measuring light scattered by NPs in a liquid medium and returns the hydrodynamic[37] size, which is increased by any coating of stabilizing agents present on the NPs, thus making the method unreliable.[38] Small angle X-ray scattering (SAXS) is another method that uses scattered electromagnetic radiation to estimate the radius of gyration[39] of NPs, but NP sizes measured by this technique are limited to about 70 nm in diameter.[40] Many other methods of determining the size of NPs also exist,[40−43] each of them with their limitations, such as price and time requirements. UV−vis $E(\lambda)$ spectra also can be used to characterize the size distribution of liquid-suspended NPs[44] but are not straightforward to interpret.[45]

The spherical NP $E(\lambda)$ spectra can be computed for a broad range of sizes either analytically employing Mie theory[36] or numerical methods.[14] Approaches based on effective media have also been developed.[46] Due to the "spectrum to distribution" problem having multiple degrees of freedom, an optimization-based approach[47] might fail to provide an optimal distribution.[48] Therefore, a more reliable approach for elucidating the size distributions from the $E(\lambda)$ spectra of NPs is required.

NP concentration is another property of interest, especially for those who develop new wet-chemistry colloidal NP synthesis methods.[49,50] NP seed solutions concentration determination is paramount for computing volumes and chemical precursor concentrations needed to produce specific-size NPs via the seeded-growth method.[51] Rapid *in situ* determination of concentration using spectroscopic data is of particular interest.[52]

In recent years, machine learning (ML)-based data analysis tools have exploded in popularity.[53] As a data-driven approach, an ML algorithm can learn the underlying patterns in the data and approximate them effectively, circumventing computational or analytical difficulties.[54,55] Recently, ML has emerged as a popular method for the characterization of particle size distributions.[56,57] Some authors use preprocessing of $E(\lambda)$ spectra in order to increase the accuracy of ML algorithms,[57] while others use the raw spectra.[44] Using computationally derived data to train ML algorithms has also drawn attention.[56,58] ML tools such as deep neural networks (DNNs) have been proven to be exceptionally powerful.[59] Due to the wide functionality of DNNs,[60] they have found many scientific applications in biomedicine,[61] materials science,[62] detection of chemical materials,[63] and many more fields, including design of NP colloids,[64] and assisting in their synthesis.[65,66] Early attempts at using multilayer feedforward DNNs to analyze particle sizes focused on the microparticle size range.[67−70] In later years, both DNNs and other ML techniques were used to investigate size distributions of particles in the nanoscale,[71] including more complex shapes such as rod-like NP,[56,72] but their success was limited at best. Essentially, determining the size distribution from an $E(\lambda)$ spectrum is an inverse modeling problem. A tandem deep neural network (DNN) approach is used quite often for solving inverse problems, for example in photonic design.[73−76]

In this work, we present a tandem DNN architecture for determining the radius distribution of seeded-growth synthesized silver (Ag) colloidal NPs as well as their concentration in the colloid from UV−vis $E(\lambda)$ spectra. The DNNs were trained by using computationally generated data composed of NP distributions, concentration values, and $E(\lambda)$ spectra. The data was engineered to be as bias-free as possible by thoroughly examining the influence of data parameters on the characteristic aspects of the data and selecting said parameters to produce unbiased data instances for the training data. The tandem DNN was tested with experimental wet-chemistry synthesized NP data, providing an excellent match between predictions and empirical results. The first stage of the tandem DNN processed the spectra by first isolating the dipolar peak of the spectrum and the second stage performing the prediction. Using the selected tandem architecture, we have demonstrated that accurate predictions of NP size can be made in a broad range — from 1 up to 150 nm in radius, which is more than reported previously in ref 57, by using dipoles by using only dipole, instead of dipole and quadrupole, features. What is more, our approach allowed to estimate the concentration of both the total mass of Ag and the Ag NP concentration in the solution.

METHODS

Experimental Methods. *Synthesis of NPs.* Ag NPs were synthesized using the seeded-growth method[8] (Figure 1a). The size and size dispersion of Ag NP seeds were controlled by varying the concentrations of trisodium citrate (TC, C_{TC}), tannic acid (TA, C_{TA}), and silver nitrate (SN, C_{SN}) (all from Sigma-Aldrich) in aqueous solution. Ag NPs were grown from seeds (Figure 1b) and enlarged in sequential synthesis steps (Figure 1c). More details on both seeds and NP synthesis are provided in Section S1.1. Six different NP colloid batches ("A"−"F") were produced as summarized in Table S1. Batches "A"−"E" were synthesized using varying concentrations of TA in the seed solution to induce NP growth, resulting in a greater variation in their size distribution. On the other hand, NPs from batch "F" were synthesized with a reduced TA concentration in the seed solution, aiming for a decrease in the concentration of components during the growth process for approaching consistent NP growth and maintaining a constant standard deviation in radii. The production of a wide variation in NP sizes, along with varying size distributions, served as a means to validate the proper functionality of the DNNs.

Characterization of NPs. UV−Vis Spectroscopy of Ag Colloids. A 1.4 nm spectral resolution optical fiber spectrometer "AvaSpec-2048" (Avantes) and light source "AvaLight-DHc" (Avantes) were used for measuring the $E(\lambda)$ spectra of colloid solutions in a 1 mm optical path length quartz cuvette. Initially, colloids were measured with their original particle concentration. All $E(\lambda)$ measurement results were normalized to $E(\lambda)$ of the same cuvette filled with water. All colloids were sonicated prior to UV−vis measurement in order to break up possible agglomerates.

Determination of NP Size Distribution. Before imaging, the NP colloids of their original concentration were sonicated in order to break up possible agglomerates. Before drop-casting of NPs for imaging, the colloid solution was processed in order to remove the TC surfactant. 100 μL of the original solution was centrifugated at 7000 rpm for 7 min. After centrifugation, the solution-supernate was replaced with 100 μL of ethanol, and the mixture was sonicated and centrifugated at the same parameters. This procedure was repeated twice, and after the second centrifugation in ethanol, the sediment was extracted and placed on a piece of silicon wafer. Each NP sample was prepared for scanning electron microscopy (SEM) imaging by drop-casting

https://doi.org/10.1021/acs.jpcc.4c02459
J. Phys. Chem. C 2024, 128, 9662−9675

the corresponding colloid solution on a silicon substrate. Field emission gun SEM "Quanta 200 FEG" (FEI) was used. Multiple micrographs of NPs from every sample were made in order to obtain a sufficient amount of NP images for a reliable effective NP radius statistical analysis. Effective Ag NP radius distribution was derived from SEM micrographs employing an automated custom micrograph analysis and statistics processing script that was implemented in MATLAB (MathWorks), similar to ref.[34] The principle of SEM micrograph pre- and postprocessing is showcased in Figure 1d—the red outline shows the actual contour of the NPs, while the green outline is the circle with the resulting effective NP radius. The steps of the automated analysis are depicted in Figure S1 and described in more detail in Section S1.2. The hydrodynamic particle radius and its distribution were also confirmed by DLS employing a "Zeta Sizer Ultra" particle size analyzer (Malvern Panalytical). Details of the measurement can be found in Section S1.3.

Determination of NP Shape and Crystallinity. A high-resolution transmission electron microscope (TEM) "ARM-200F" (JEOL) was used for imaging Ag seeds and NPs. NPs were prepared for imaging by casting them on a TEM wire grid and then drying them at room temperature. Due to the higher magnification of the TEM when compared to SEM, TEM micrographs were used for NP shape and qualitative crystallinity inspection purposes. The crystallinity of several selected samples was also evaluated by X-ray diffraction (XRD) using an "X-ray diffractometer D8 Discover" (Bruker AXS GmbH). Measurement details can be found in Section S1.4.

Concentration Measurement of Colloids. Atomic absorption spectrometer "AAnalyst 400" (PerkinElmer) was used to measure the mass concentration (mg/L) of Ag in the Ag NP colloids. Colloid samples were specially prepared before measurement—Ag NPs were dissolved in Aqua Regia mixed in a ratio of 2:1.

Numerical Methods. *Computing Hardware and Software.* A desktop computer with a processor "Intel(R) Core (TM) i5-9500 CPU@3.00 GHz" and 16 GB of RAM running "MATLAB 2021a" (MathWorks) on "Windows 10 Enterprise" (Microsoft) was used to perform all computations. Training of the DNNs as well as their hyperparameter optimization was performed on the same computer using a graphical processing unit (GPU) "GeForce GTX 1050 Ti" (NVIDIA).

Mie Theory for the Calculation of Full Extinction Spectra. Mie theory, as described in ref 36, was used to compute the $E(\lambda)$ of spherical NPs. The spectra $E(\lambda)$ contained peaks corresponding to all resonances depending on the NP size, not just the dipolar ones. Such spectra in this work are termed full spectra (Figure 1f blue spectra). The NP distributions used to originate full spectra were the same as those used for the dipole spectra. In Mie theory, the amplitude of $E(\lambda)$ is defined by the number of NPs (N) interacting with the light wave and the thickness of the interaction region (constant in our case). The Palik permittivity was used to define the Ag NPs,[77] while the permittivity of water was taken from ref 78.

Transfer Matrix Method (TMM) Using Effective Medium Theory for the Calculation of Dipolar Extinction Spectra. The Transfer Matrix Method (TMM)[79] based on scattering matrices[80] was used to compute $E(\lambda)$ containing only dipolar resonances corresponding to $E(\lambda)$ peaks of spherical NPs. In this work, such spectra are termed dipole spectra (Figure 1f green spectra). Since TMM is only able to perform computations on homogeneous slabs of material, a modified Maxwell−Garnett−Mie (MMGM) effective medium theory (EMT)[46] was used to homogenize the colloidal solution of randomly distributed subwavelength-sized NPs into a homogeneous medium (Figure 1f). The same permittivity dispersions were used as in Section 2.2.2. Using an EMT allows one to avoid a generally computationally intensive and time-consuming 3D numerical simulation. This was extremely useful for generating training and validation data in vast quantities. The effective medium approximation is valid as long as the NPs are of sufficiently subwavelength size.[81] The effective medium model and its validity for larger NPs are described in more detail in Section S1.5.

In MMGM, the concentration is accounted for as a volume-filling fraction (F). The concentration of NPs in the colloid directly impacts the amplitude of the modeled spectra, with a higher concentration corresponding to a higher amplitude as explained in detail in Section S2.5.

Engineering of Training and Validation Data. Using Mie theory for full spectra and TMM with MMGM medium for dipole spectra, NP distributions and the corresponding $E(\lambda)$ spectra were synthetically generated for both training and validation of DNNs. Assuming the log-normal shape of NP size distributions, the mode (M_L) and full width at half-maximum ($\mathrm{fwhm_L}$) were selected as the parameters defining the distribution. Due to the lack of a parametrization of log-normal distributions with these parameters, they were subsequently transformed into canonical parameters, mean μ_L, and standard deviation σ_L, which were used to generate the distributions. The derived equations of the transformation (eqs S4 and S5) are provided in Section S1.6, while the ranges of all data parameters are found in Table S2.

Two sets of computationally derived training and validation data were generated: one for DipoleNet and one for ColloidNet. For DipoleNet, data consisted of pairs of full spectra (inputs, Figure 1f blue spectra) and the corresponding dipole spectra (outputs, Figure 1f green spectra). For ColloidNet, data pairs were composed of dipole spectra and the corresponding NP distributions along with their F values (Figure 1f red distribution). The size of each training data set was 626,359 pairs, while the size of each validation data set was 156,590 pairs—1/4th the size of the training data.

Testing data for DipoleNet used experimentally obtained full $E(\lambda)$ spectra for the inputs. For the output, the best dipole spectrum fits, computed with TMM using MMGM medium, for the dipolar resonance peak of full spectra were used. Testing data for ColloidNet consisted of dipole spectra obtained from DipoleNet for the inputs and experimentally obtained distributions of the effective NP radius and NP colloid concentration measurements for the outputs. Each testing data set consisted of 45 corresponding pairs.

Architecture of Neural Networks, Hyperparameter Optimization, and Network Training. DNN DipoleNet is constructed as a multilayer feedforward neural network and is depicted in Figure 1e. It is composed of an input layer, internal blocks of layers, and an output layer. A fully connected layer followed by a Leaky ReLU activation function constitutes a single block. The Leaky ReLU function was chosen to avoid the vanishing gradient problem.[82] Finally, a regression layer was used as the output layer.

Similarly, ColloidNet, depicted in Figure 1e, was also composed of an input layer, repeating layer blocks, and an output layer. This time, a single block was composed of a fully connected layer, a normalization layer, a Leaky ReLU layer, and a dropout layer. Descriptions of all layers are available in ref 83.[83]

https://doi.org/10.1021/acs.jpcc.4c02459
J. Phys. Chem. C 2024, 128, 9662−9675

To determine the best hyperparameters,[84] hyperparameter optimization (HPO) using Bayesian optimization[85] was performed. The numbered workflows of HPO for both DNNs are depicted in Figure 1g. For DNN training during HPO, 1/10th of the training and validation data sets are randomly extracted into reduced training and validation data sets. Validation root-mean-square error (RMSE) was chosen as the cost function to minimize. The reduced data sets were reshuffled once every epoch to ensure maximum data variation during training. It is assumed that hyperparameters that ensure the best network performance (lowest validation root-mean-square error, RMSE) will also provide the best network performance when training and validating the DNN with full-sized data sets. It was empirically determined that the root-mean-square propagation training algorithm[86] works best for training both DNNs. After HPO, optimal hyperparameters were used to train and monitor the DNNs with their respective full-sized training and validation data sets. The same training parameters that were used during the HPO were used for the final training process. Ranges of hyperparameters, along with optimal values and other parameters of both DNNs are listed in Table S3. The use of training and validation data during training is described in Section S1.7.

RESULTS AND DISCUSSION

Experimental Results. Overall, 45 Ag NP samples were synthesized via the seeded-growth method (Figure 1a–c).[8] NPs were specifically synthesized to have two distinct kinds of distributions, narrow distributions and broad distributions, for various mean radius ranges. This distinction between different batches is clearly visible in the distributions of their statistical parameters, depicted in Figure S2 and available in Table S1. From these empirical data, it was observed that radius distributions with a smaller mean NP radius are narrower, while distributions with a larger mean NP radius are broader. This directly translates into full width at half-maximum (fwhm) of the log-normal fits and is consistent with experimental data provided by other authors.[8] Meanwhile, NP radius distributions (histograms of probability density with a bin width of 1 nm) for all samples (sorted by the mean NP radius) are displayed in Figure 2e. Mean NP radius values in the study span from 10.5 to 107.6 nm. On average, around 1000 (and sometimes up to ca. 2000), but never less than 600, NPs are observed for each NP sample, providing high reliability of the collected statistics of NP radius distributions as recommended by the literature.[87] The strong reliance on a number of NPs imaged for obtaining accurate size distributions is one of the biggest drawbacks of direct imaging methods like SEM or TEM. The SEM-measured NP size distributions were verified by TEM analysis and indicated a good overall match between the results, but due to a significantly smaller number of NP samples analyzed, they were not used further and are not shown here. Based on the goodness of fit being $R^2 > 0.87$ for all samples, it was confirmed that the NP radius distributions have a log-normal distribution. Such observation is consistent with the literature.[11,12] Another drawback of direct imaging techniques like SEM is that the mean size of NPs is subject to shifting depending on how the micrographs are analyzed. Finally, NP samples can require specific preparation such as surfactant stripping or sonication, both of which were used in order to obtain the best possible results from SEM.

Because imaging-based measurement techniques (TEM, SEM) determine the size of each NP directly, the quality/noise of the underlying distribution shape and reliability of statistical parameters derived from the said distribution are affected by the number of NPs that are analyzed. Indirect measurement methods such as DLS[36] produce smooth NP distributions. They confirmed the tendency of the electron

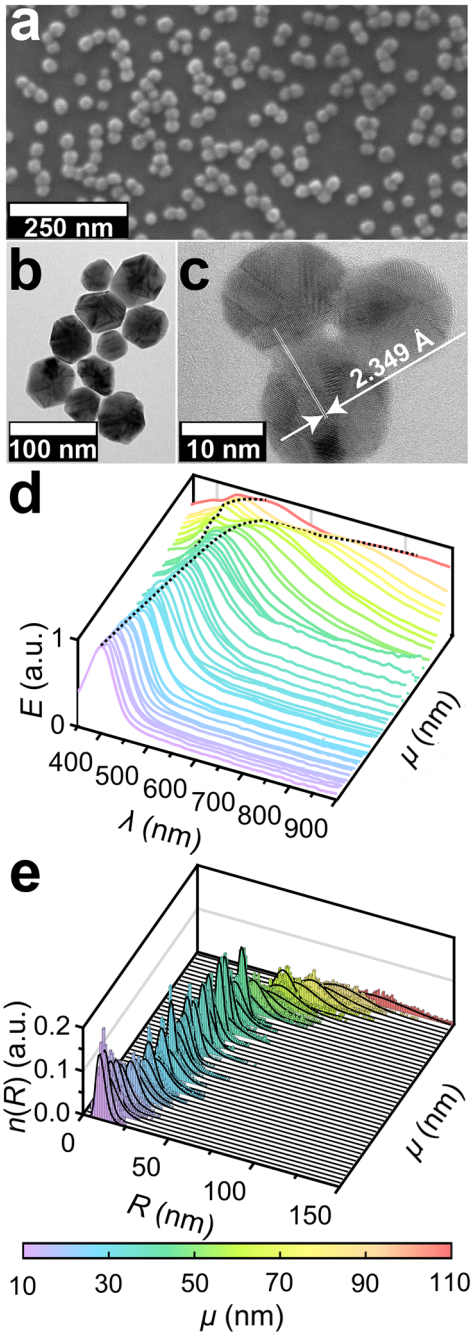

Figure 2. Properties of the synthesized Ag NP colloids. (a) Typical SEM micrograph of Ag NPs from a drop-cast colloidal solution on a silicon substrate (sample "C5"). (b) TEM micrographs of NPs after several stages of growth (sample "F15"). (c) High-resolution TEM micrographs of NP seeds for the F batch, showing the crystallite boundaries of the NP seeds with indicated interatomic distance corresponding to the Ag(111) plane. (d) $E(\lambda)$ spectra, normalized to one, of all investigated colloidal solutions with increasing mean NP radius; truncated lines indicate dipole and quadrupole peak positions. (e) NP radius distributions corresponding to the spectra in panel (d) extracted from the SEM micrographs; a solid line represents the log-normal fit of experimental distribution.

https://doi.org/10.1021/acs.jpcc.4c02459
J. Phys. Chem. C 2024, 128, 9662−9675

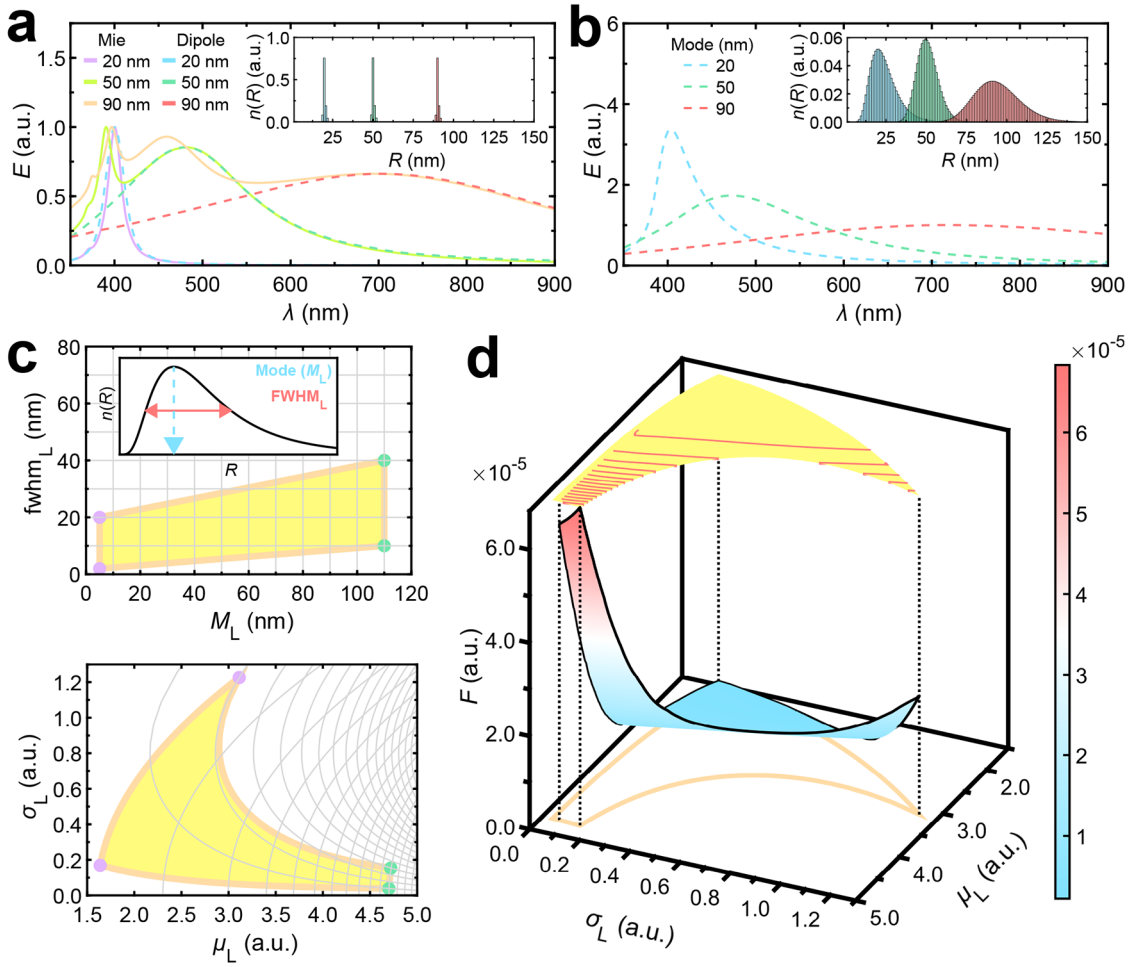

Figure 3. Training data for DNNs. (a) Comparison of $E(\lambda)$ full spectra originated with Mie theory (solid lines) and dipole spectra originated with TMM using MMGM medium (dashed lines), the inset depicts narrow radius distributions (M_L 20, 50, and 90 nm, fwhm_L 5 nm) used to compute $E(\lambda)$ spectra employing both origination methods. (b) Dipole $E(\lambda)$ spectra for broad radius distribution NPs with M_L identical to those used in panel (a), depicted in the inset. Spectra were computed with TMM using MMGM medium, where the volume-filling fraction doubles for each subsequent distribution. (c) Log-normal distribution parameter (M_L and fwhm_L) values in the training data before and after transformation to canonical distribution parameters μ_L and σ_L. (d) Values of filling fraction F depending on canonical distribution parameters required for achieving the amplitude of the dipole E(λ) spectrum equal to one.

microscopy results, but despite that, DLS-determined size distributions did not always absolutely overlap with electron microscopy results (Figure S3) and were suboptimal for DNN validation as explained in more detail in Section S2.2.

Both transmission and scanning electron microscopies confirmed that the NP seeds were spherical (Figure 2a) and became more faceted as NPs grew (Figure 2b) but in general preserved a symmetrical close to spherical shape, hence suitable to be described by the MMGM effective medium theory.[46] This is consistent with the literature describing the synthesis of spherical Ag NPs using various wet chemical methods.[88−91] In Figure 2c, the crystallite planes corresponding to the Ag(111) facet can be attributed to sub-NP-sized crystallites that constitute the polycrystalline NPs and are larger for bigger radius NPs (Figure S4), as discussed in more detail in Section S2.3.

$E(\lambda)$ spectra following the same increasing mean NP radius order are displayed in Figure 2d. For narrow NP distributions with a small mean NP radius, the $E(\lambda)$ spectrum consists of a single narrow peak, corresponding to a dipole resonance.[92] As the mean NP radius increases, the peak $E(\lambda)$ wavelength shifts toward longer wavelengths, and the fwhm of the $E(\lambda)$ peak increases due to dynamic effects.[46] In general, the $E(\lambda)$ spectrum is composed of a multitude of resonances (Figure S5a), but for small NPs, only dipolar resonances manifest. As NP size increases, higher-order LSPR oscillations become supported; a quadrupole $E(\lambda)$ peak emerges and continues to grow in intensity, peak position, and fwhm, eventually overtaking the dipole peak's intensity (Figure S6b). These findings are consistent with widely known predictions made with Mie theory reported by other authors, e.g., see refs 36,93. Once higher-order modes are supported, the quasi-static approximation[16] no longer holds. At that point, scattering is the dominant factor of $E(\lambda)$ (Figure S6a). However, this transition is not clear-cut, as determined in ref 81. In our work, it was found that the MMGM effective medium theory is still valid even for NPs with a radius of 150 nm as long as F is increased to account for the loss of amplitude. For a more in-depth discussion about the validity of the effective medium theory used for generating synthetic $E(\lambda)$ spectra, see Section S2.4.

Numerical Data Results. Using eqs S4 and S5 and numerically derived relationships of F (eq S6) and N (eq S8), data instances were engineered to be as bias-free as possible by selecting the ranges of the underlying data values to correspond

https://doi.org/10.1021/acs.jpcc.4c02459
J. Phys. Chem. C 2024, 128, 9662−9675

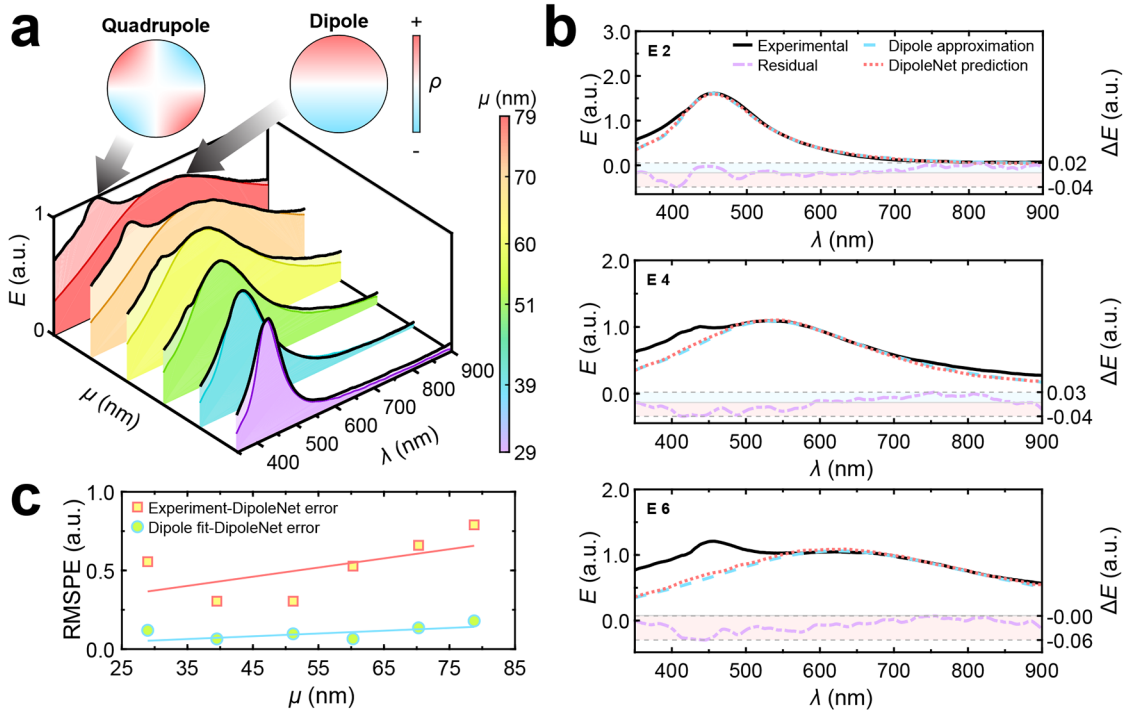

Figure 4. Extraction of a dipole component from full $E(\lambda)$ spectrum. (a) Examples of full spectra (light shade) and dipole spectral components (dark shade with dashed line) for the "E" batch of colloid solutions increasing in mean NP radius extracted with DipoleNet, along with surface charge density distributions corresponding to distinct resonances. (b) 2nd, 4th, and 6th spectra from panel (a) compared with dipole spectra predicted by DipoleNet and dipole spectra computed with effective medium theory and TMM for the best fit of the dipole spectral peak on the primary axis and the difference between the dipole spectrum and predicted spectrum of DipoleNet on the secondary axis. (c) RMSPE between full $E(\lambda)$ spectra and DipoleNet predicted $E(\lambda)$ spectra compared to the error between DipoleNet spectra and dipole spectra for various mean NP sizes.

to those of testing data and by equally representing all cases of data values in those ranges (Table S2). The relevant data parameter region in the (M_L, fwhm$_L$) space is depicted in Figure 3c (top), and the same region posttransformation in the (μ_L, σ_L) parameter space is depicted in Figure 3c (bottom). Due to the logarithmic nature of the log-normal distribution parameters (μ_L, σ_L), the posttransformation region is spaced unevenly compared to the linear (M_L, fwhm$_L$) space.

The effect of (μ_L, σ_L) on F in MMGM when the spectrum amplitude is maintained is highly nonlinear, as depicted in Figure 3b and in Figure 3d in more detail. An equivalent relation also exists for N in the Mie theory. This was taken into account when generating training and validation data. It is observed that for larger NPs, F has to increase tremendously in order to preserve the amplitude. This is because the absorbance cross-section decreases in relation to the $E(\lambda)$ cross-section due to the onset of scattering (Figure S6). That is why the same value of F produces a smaller amplitude of the spectrum for larger NPs as computed with TMM and MMGM because MMGM computes absorbance and is based on the first (dipolar) electric Mie coefficient. However, this change in amplitude does not have any effect on the shape of the spectrum as it is an extremely close match when the relevant peak of full and dipole $E(\lambda)$ spectra is brought to the same amplitude (Figure 3a). Due to the effect of F weakening with increasing NP size, it needs to be increased in order to maintain the same spectrum amplitude. Knowing the dependence of F on the $E(\lambda)$ amplitude to be directly proportional,[46] this dependence is universal for any spectrum amplitude. An analogous dependence was determined for N, which is a parameter in Mie theory that is equivalent to F in MMGM. Due to scattering being accounted for in Mie theory, the dependence of N was different than that of F. Both of these dependencies were used to generate synthetic spectra with amplitude changes in an exact manner. This allowed for the generation of training and validation data with a high amount of variation and virtually no bias.

Due to the dependence depicted in Figure 3d being derived numerically, it could not be used as a general expression, which is crucial for generating the F value for any given parameters (μ_L, σ_L). Therefore, it was fitted using a two-variable fifth-order polynomial fit, with the goodness of fit parameter R^2 being 0.999. For the actual application, the fit of F was used to compute the value of F for log-normal distributions with the parameters (μ_L, σ_L).

It should be noted that NPs have a certain lower size limit, where they transition into clusters, properties of which are quantum in nature. This transition is usually considered to happen at ca. 1 nm radius[94−97] (see Section S1.5 for more details), and hence it is the smallest radius value chosen to be predicted by the tandem DNN.

DipoleNet DNN Results. The results of the DipoleNet tests are summarized in Figure 4. It is important to mention that the output of DipoleNet is purely fictitious as there are no real dipole E(λ) spectra[98] and is only used as a stepping stone for achieving the end result—the output of ColloidNet. During the operation of the tandem DNN, this output is further used as the input for ColloidNet.

As seen in Figure 4a, the $E(\lambda)$ peak, which corresponds to higher-order charge oscillations, is becoming more prominent with increasing NP size. The results of using DipoleNet on its testing data can be seen in Figure 4b. The residual between the dipole fit spectrum and the prediction of DipoleNet at most is

https://doi.org/10.1021/acs.jpcc.4c02459
J. Phys. Chem. C 2024, 128, 9662−9675

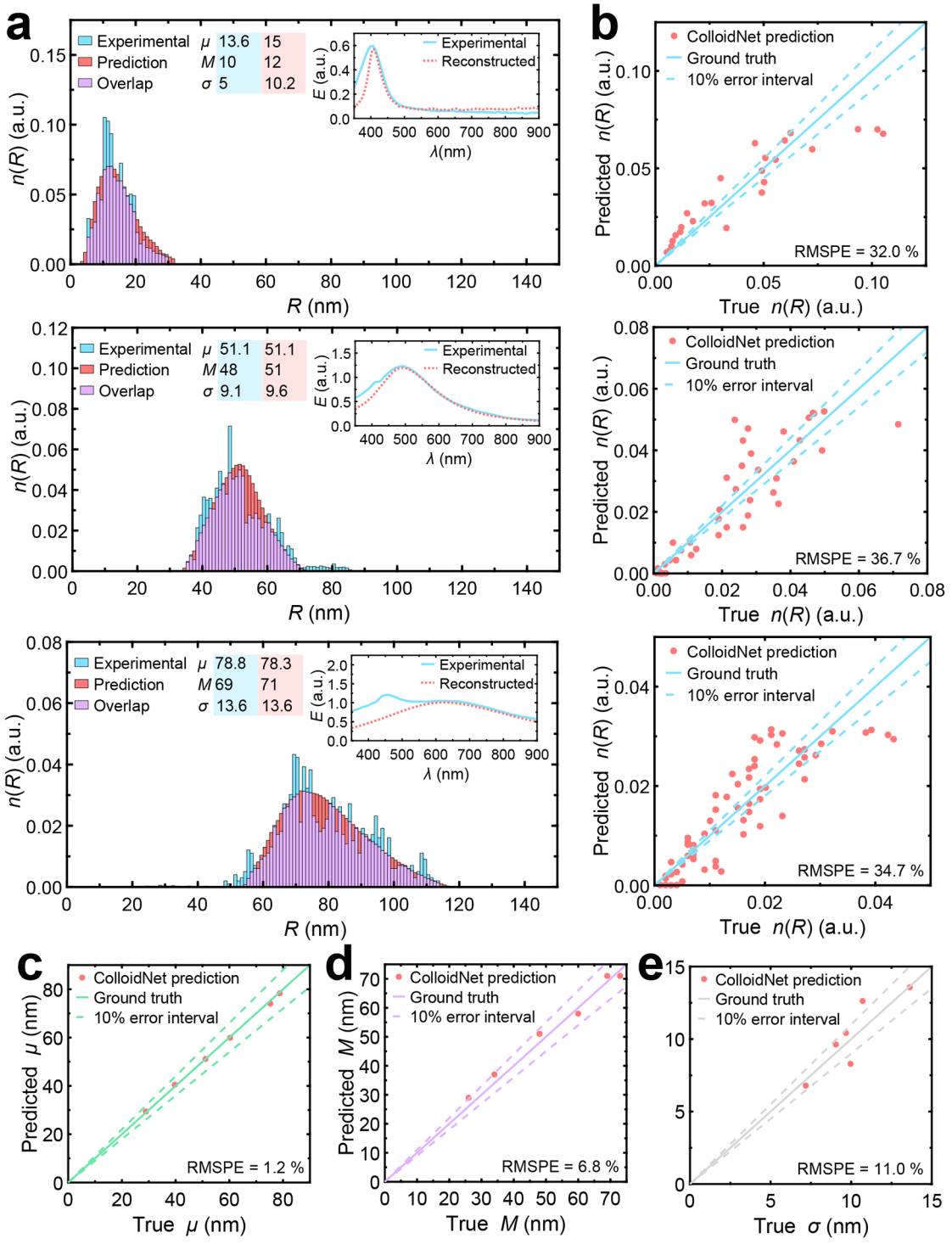

Figure 5. Comparison of NP size distribution characterization by SEM and ColloidNet. (a) Experimental and predicted NP size distributions and their statistical distribution parameters for samples "F2", "E3", and "E6"; the inset depicts experimental $E(\lambda)$ spectra and dipole spectra reconstructed from the predicted NP distributions and their volume-filling fractions. (b) True−predicted value plots for distributions of panel (a) with the estimated RMSPE values and 10% absolute error intervals (dashed lines). True−predicted value plots for mean NP sizes (μ), modes (M), and standard deviations (σ) and their respective RMSPE values for distributions of colloid series E are depicted in panels (c), (d), and (e), respectively, with solid lines corresponding to the true value, while dashed lines correspond to a 10% absolute error interval.

about two orders of magnitude less than the $E(\lambda)$ amplitude, which corresponds to an absolute error of a few percent at most. This indicates that the DipoleNet has correctly learned to predict the characteristics of the $E(\lambda)$ peak that corresponds to the dipole component of $E(\lambda)$. Furthermore, in Figure 4c, it is seen that the root-mean-square percentage error (RMSPE[99]) between the dipole fit and DipoleNet prediction is also consistently small throughout a wide range of NP radii. Not only does this further support the conclusion that DipoleNet has correctly learned to identify the dipole feature but it also shows

https://doi.org/10.1021/acs.jpcc.4c02459
J. Phys. Chem. C 2024, 128, 9662−9675

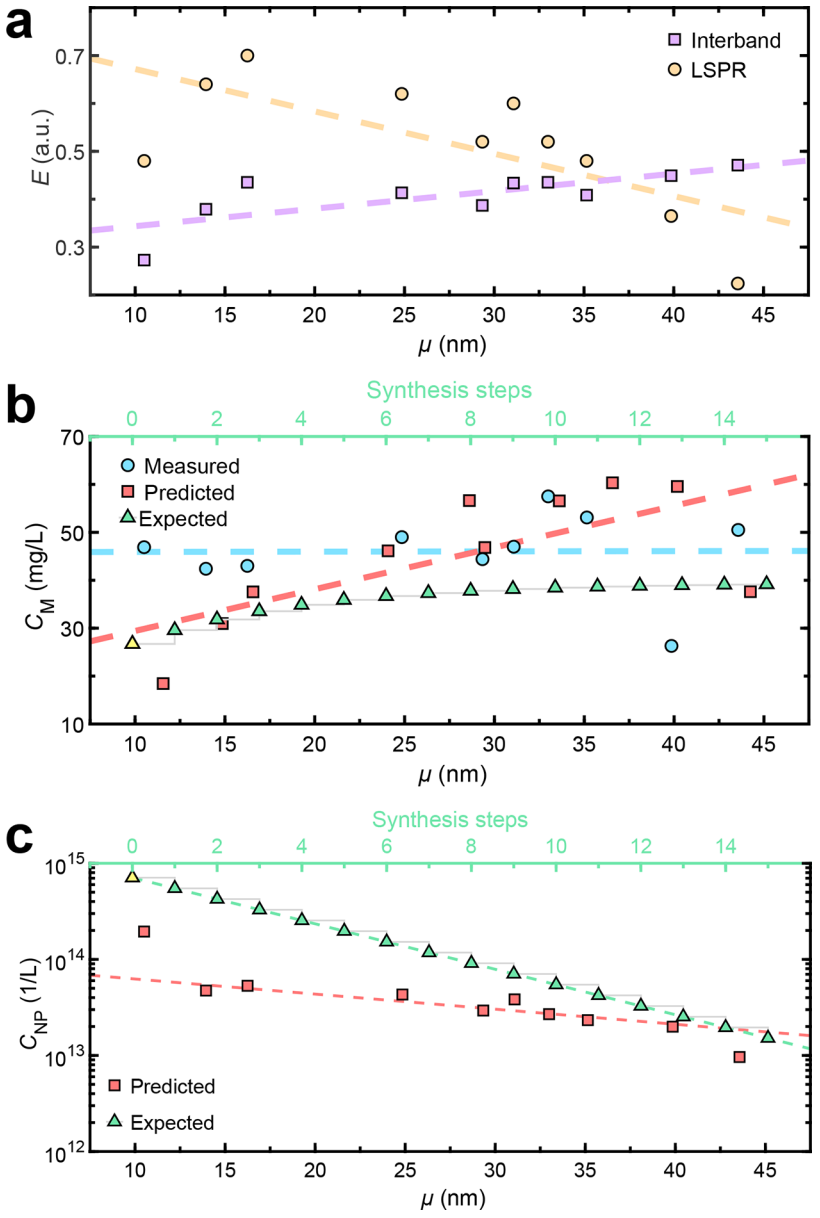

Figure 6. Concentration estimates for selected colloids of the F batch. (a) Trends of experimental $E(\lambda)$ of the interband transition (at 250 nm) and the LSPR peak found in Figure S7a. (b) Experimental vs predicted vs. expected mass concentration (C_M). (c) ColloidNet predicted NP concentration (C_{NP}) vs expected NP concentration assuming monodisperse NPs, 8 nm seeds, and 40% reaction efficiency with seed concentration 7.088×10^{14} and Ag density 10.49 g/cm^3. The first "expected" values in panels (b) and (c) indicated in yellow are NP seeds. Lines are guides for the reader's eye.

the network's reliability for NPs of various sizes. DipoleNet conducted each individual prediction in about 0.0031 s.

ColloidNet DNN Results. *Predictions of NP Size.* The DipoleNet-processed experimental $E(\lambda)$ spectra were fed as inputs to ColloidNet and resulted in the NP size predictions depicted in Figure 5. Similar to DipoleNet, ColloidNet originated its predictions in ca. 0.0082 s per spectra. As seen in Figure 5a, all distributions have a clearly defined log-normal nature.[11] By mere visual inspection, it can be seen that the shape of the predicted distributions is close to empirically determined NP radius distribution, indicating that ColloidNet predictions are correct. The main source of mismatch between the ground truth (experimental data) and network predictions seems to be noise due to having a limited number of samples as ca. 1000 NP radius data points might still be not enough to produce a smooth histogram and/or possible analysis errors of the automated SEM micrograph processing algorithm. There are two possible error types in the micrograph processing algorithm—(i) over-segmentation of NPs when one NP is misunderstood as several smaller ones and (ii) nonseparation where several NPs clumped together are misunderstood as one large NP. Both can arise due to using the watershed transformation[100] to separate the NPs clumped together in the micrographs.

The true-predicted plots corresponding to the three analyzed histograms in Figure 5a are depicted in Figure 5b. They confirmed a good correlation between the predicted values and the ground truth. Most points follow the trend of this line, while overestimates of the histogram bins are above the ground truth line and underestimates are below. These errors mostly represent the smallest values of $n(R)$ (see Figure 5b) that are less significant as they have little contribution to $E(\lambda)$. It can be further seen that for distributions with increasing mean NP size,

https://doi.org/10.1021/acs.jpcc.4c02459
J. Phys. Chem. C 2024, 128, 9662−9675

the RMSPE is consistently under 50%, indicating the ColloidNet has a similar level of prediction accuracy for NPs over a broad size range. Additional results of Ag NP size prediction for "C" series (Figure S8) and for the mean size of all investigated colloids (Figure S9) can be found in Section S2.6.

The quantitative statistical distribution parameters—the mean (μ), mode (M), and standard deviation (σ)—for both experimental and predicted distributions are provided in Figure 5a legend for selected cases and also analyzed for the entire batch E in Figure 5c−e, respectively, indicating excellent agreement between predicted and experimental values. The mean μ was predicted with the highest level of accuracy, while M was slightly underestimated. Haiss et al.[101] proposed a highly simplified method for determining mean NP sizes from their dipolar $E(\lambda)$ peak spectral location, but it makes no effort to account for the shape and especially the size distribution width. Meanwhile, σ had the largest deviation from the ground truth and was always overestimated. Overestimation of the σ values can be explained by the noise in network predictions. Although not visible in the histograms due to its small size, predictions made with ColloidNet contain low amplitude noise, which could have influenced the estimate of σ. Another possibility is that NPs much larger or smaller than the mean values were simply not observed due to an insufficient number of NP radius samples, as it would require using tens or hundreds of thousands of samples to observe them because they are just that rare. Still, value prediction is consistently accurate over a large interval, and in most cases, the parameters are within 10% RMSPE bounds or even as small as 1.2% for μ of large NPs. The overall prediction accuracy for μ in the study was 6.1% (Figure S9) and was consistently better for larger NPs. This shows the versatility of the proposed tandem DNN system. Shiratori et al.[56] reported a similar prediction accuracy level for the nanorod sizes. This work has the advantage over ref 71 because here size characterization is achieved only from UV−vis $E(\lambda)$ spectra, without requiring DLS data as input. Moreover, to the best of our knowledge, the current work exceeds the maximum plasmonic NP radius prediction range of 110 nm previously reported by Tan et al.[57] by at least 40 nm. Higher prediction accuracy without sacrificing the prediction range could potentially be achieved by using empirical $E(\lambda)$ spectra as training data, but this requires the synthesis of tens if not hundreds of colloids with precision NP size tuning and concentration increment.[57] Moreover, the current study was limited by the spectral range of the silicon-based detector spectrometer and deuterium−tungsten light source, while the LSPR range together with mean sizes could be potentially extended using a multiple detector UV−vis−NIR spectrometer. Using both dipolar and quadrupolar features/spectra could potentially yield an even wider window of size characterization,[57] but it would require discarding the use of the effective medium theory that brought computational benefits met in this work.

The insets of Figure 5a depict the full experimental UV−vis $E(\lambda)$ spectra along with the DNN-predicted dipole spectra, while it is a direct computation result of the ColloidNet predicted parameters, NP radii distributions and their respective volume-filling fractions. The shape of the dipole peak is mainly affected by the NP radius distribution shape, while the amplitude of the peak is affected by the filling fraction, which is equivalent to the NP concentration. A good fit of the dipole peak is one more quality estimation metric indicator that the prediction is correct or close to it, especially in terms of concentration.

Predictions of NP Concentration. Since ColloidNet predicts only the volume-filling fraction F, additional postprocessing is needed to convert it into useful parameters such as Ag mass (C_M) and NP (C_{NP}) concentrations as explained in Section S2.5. Predictions of F batch NP colloid Ag concentration acquired from ColloidNet predictions are depicted in Figure 6. For ColloidNet, the LSPR $E(\lambda)$ peak magnitude is the key factor for predicting both C_M and C_{NP}, due to it being directly influenced by F (eqs S7 and S9), according to ref 46. However, the influence of the size distribution $n(R)$ becomes significant when computing C_{NP}, as it is directly impacted by the NP size (eq S9).

The literature described a relation between the intensity of $E(\lambda)$ at the interband wavelength that is 250 nm for Ag and the overall concentration of the material in the colloid.[102,103] Therefore, the dependence of the $E(\lambda)$ magnitude at the interband together with the maximum position of the LSPR on the mean NP radius is depicted in Figure 6a. The slightly increasing interband trend (Figure 6a) can be directly addressed with the stepwise Ag precursor addition at each NP synthesis. The interband $E(\lambda)$ is indicative of the overall Ag present in the solution (C_M), not just the Ag that is in NP form and follows the expected $AgNO_3$ content trend (Figure 6b) computed based on synthesis conditions tabulated data in Table S1. Moreover, the predicted C_M is at the very same absolute mg/L level as expected based on the used chemical synthesis recipe and confirmed by the independent atomic mass spectroscopy measurement.

Finally, C_{NP} can be computed from C_M (Figure 6c) and compared with an expected value, which is computed from the synthesis conditions, assuming the silver precursor is uniformly distributed among all NPs.[51] This is described in more detail in Section S2.5. It is important to note that expected C_{NP} values are computed by assuming the NPs are monodisperse, while predicted C_{NP} values have the distribution predicted by ColloidNet. It is evident that dilutions of the colloids in each growth step play a key role in the decreasing trend of both predicted and expected C_{NP} and are the ultimate cause of the decrease of $E(\lambda)$ relating to the LSPR peak as depicted in Figures 6a and S7a. This is mainly because the decrease in the number of NPs cannot be compensated for by the increase in the scattering component (Figure S6a), causing a net decrease in $E(\lambda)$. A very similar LSPR peak trend (Figure S7b) was observed by others as well.[8] While the decreasing C_{NP} may seem like a quirk of the seeded-growth synthesis method, dilution of the colloid used as a seed solution for the next growth step is paramount in order to ensure adequate growth of NPs—otherwise, the NPs are observed to hardly grow at all, even after multiple growth steps.[51] The NP size estimations in the seeded-growth synthesis often assume 100% consumption of the Ag precursor,[51] while in our case, around 40% provided a close result in the semilogarithmic plot depicted in Figure 6c. A closer to unit consumption might be expected if the NP distribution was taken into account, while here size distribution was not estimated at all. But the expected and experimentally obtained tendencies hold, and it for the last time here confirms that the DNN-predicted Ag concentrations are trustworthy.

Limitations of the Proposed Method. It is noteworthy that the performance of the proposed method can be affected by factors influencing the extinction spectra provided to the tandem DNN. In and of itself, DipoleNet is not affected by any factors affecting the input $E(\lambda)$ spectra—it simply recognizes and extracts the dipole component of the spectrum. However, those factors that affect the $E(\lambda)$ spectra also affect the dipole components extracted by DipoleNet. On the other hand,

https://doi.org/10.1021/acs.jpcc.4c02459
J. Phys. Chem. C 2024, 128, 9662−9675

predictions (both NP size and concentration) made by ColloidNet are influenced by factors affecting the input $E(\lambda)$ spectra. If the input spectrum is red-shifted for any reason, then the NPs will be predicted to be larger than their actual size. Red-shifting can occur due to NPs being placed in a host matrix (liquid) with a larger refractive index, having a thick coating of surfactants, or aggregation of NPs. Aggregation not only red shifts the spectrum but also decreases its magnitude. This will cause ColloidNet to evaluate the NP concentration as being smaller than it actually is. All of these factors are described in more detail in Section S1.5.

CONCLUSIONS

In this work, we demonstrated the capability of a deep tandem neural network system to perform accurate silver nanoparticle size distribution and concentration predictions using UV−vis extinction spectra as input.

Automated identification of the dipole peak contribution with the first DNN helped to accurately predict the NP size distribution with the second DNN in the wide range from 1 nm up to 150 nm retaining down to ca. 1.2% root-mean-square percentage error predicting the mean nanoparticle size.

The tandem DNN predictions allowed for attaining accurate silver mass and nanoparticle concentration tendencies, and their estimates throughout the seeded-growth synthesis steps were confirmed by the growing extinction at the interband and alternative atomic absorption measurement.

The extinction spectra computed according to the predicted nanoparticle size distributions and volume-filling fractions matched the dipolar component of the experimental extinction spectra extremely well, further indicating an accurate prediction.

It was demonstrated that high accuracy and 11.3 ms per sample prediction rate can be achieved without any spectral data processing before providing it to the tandem DNN, making the proposed approach a good candidate for real-time nanoparticle colloid characterization under both laboratory and industrial conditions.

It was verified that the plasmonic NP size limit validity for the modified Maxwell−Garnett−Mie effective medium theory is much larger than previously thought and that the theory can be reliably used to estimate the size distribution of NPs based on their optical extinction dipole peak up to 150 nm in radius.

ASSOCIATED CONTENT

Data Availability Statement

Experimental data is freely available at "Zenodo": 10.5281/zenodo.11091437. Other data can be made available after a reasonable request to the corresponding authors.

Supporting Information

The Supporting Information is available free of charge at https://pubs.acs.org/doi/10.1021/acs.jpcc.4c02459.

Details of Ag NP synthesis, volumes and concentrations of Ag NP precursors (Table S1); description of SEM micrograph analysis, example of SEM analysis (Figure S1); description of DLS measurements, description of XRD measurements, description of MMGM effective medium, parametrization of training and validation data, ranges of data parameters (Table S2); strategy of hyperparameter optimization, list of hyperparameters (Table S3); discussion about statistics of experimental data, statistical parameters of experimental data (Figure S2); discussion about DLS results, DLS results (Figure S3); discussion about XRD results, XRD results (Figure S4); XRD diffractogram parameters (Table S4); XRD crystallite size analysis (Table S5); discussion about the MMGM medium, comparison of MMGM, and Mie theory results (Figure S5); comparison of scattering and absorbance (Figure S6); discussion about the prediction of concentration, LSPR amplitude trends (Figure S7); discussion about mean size prediction trends for "C" NP batch (Figure S8); and predictions of mean size for all investigated colloids (Figure S9) (PDF)

AUTHOR INFORMATION

Corresponding Authors

Tomas Klinavičius − *Institute of Materials Science of Kaunas University of Technology, LT-51423 Kaunas, Lithuania;* orcid.org/0000-0002-7925-1691; Phone: +370 (37) 313432; Email: tomas.klinavicius@ktu.lt

Tomas Tamulevičius − *Institute of Materials Science of Kaunas University of Technology, LT-51423 Kaunas, Lithuania; Department of Physics, Kaunas University of Technology, LT-51368 Kaunas, Lithuania;* orcid.org/0000-0003-3879-2253; Email: tomas.tamulevicius@ktu.lt

Authors

Nadzeya Khinevich − *Institute of Materials Science of Kaunas University of Technology, LT-51423 Kaunas, Lithuania;* orcid.org/0000-0001-9348-3918

Asta Tamulevičienė − *Institute of Materials Science of Kaunas University of Technology, LT-51423 Kaunas, Lithuania; Department of Physics, Kaunas University of Technology, LT-51368 Kaunas, Lithuania;* orcid.org/0000-0003-4152-1382

Loïc Vidal − *Institut de Science des Matériaux de Mulhouse IS2M UMR 7361, F 68100 Mulhouse, France*

Sigitas Tamulevičius − *Institute of Materials Science of Kaunas University of Technology, LT-51423 Kaunas, Lithuania; Department of Physics, Kaunas University of Technology, LT-51368 Kaunas, Lithuania;* orcid.org/0000-0002-9965-2724

Complete contact information is available at: https://pubs.acs.org/10.1021/acs.jpcc.4c02459

Author Contributions

Conceptualization and methodology: T.K., T.T.; investigation: T.K., N.K., A.T., L.V.; data analysis: T.K., N.K., A.T., T.T.; writing—original draft: T.K., T.T.; writing—review and editing: T.K., N.K., A.T., S.T., T.T.; supervision and funding acquisition: T.T.

Notes

The authors declare no competing financial interest.

ACKNOWLEDGMENTS

The authors acknowledge having received funding from the Research Council of Lithuania (LMTLT), Agreement No. S-MIP-23-93. The authors especially thank Dr. Karine Mougin from the Institut de Science des Matériaux de Mulhouse IS2M UMR for the technical assistance with DLS measurements.

REFERENCES

(1) Khan, I.; Saeed, K.; Khan, I. Nanoparticles: Properties, Applications and Toxicities. *Arabian J. Chem.* **2019**, *12*, 908−931.

(2) Vert, M.; Doi, Y.; Hellwich, K.-H.; Hess, M.; Hodge, P.; Kubisa, P.; Rinaudo, M.; Schué, F. Terminology for Biorelated Polymers and Applications (IUPAC Recommendations 2012). *Pure Appl. Chem.* **2012**, *84*, 377−410.
(3) Ijaz, I.; Gilani, E.; Nazir, A.; Bukhari, A. Detail Review on Chemical, Physical and Green Synthesis, Classification, Characterizations and Applications of Nanoparticles. *Green Chem. Lett. Rev.* **2020**, *13*, 223−245.
(4) Xing, T.; Sunarso, J.; Yang, W.; Yin, Y.; Glushenkov, A. M.; Li, L. H.; Howlett, P. C.; Chen, Y. Ball Milling: A Green Mechanochemical Approach for Synthesis of Nitrogen Doped Carbon Nanoparticles. *Nanoscale* **2013**, *5*, 7970.
(5) Salavati-Niasari, M.; Davar, F.; Mir, N. Synthesis and Characterization of Metallic Copper Nanoparticles via Thermal Decomposition. *Polyhedron* **2008**, *27*, 3514−3518.
(6) Amendola, V.; Meneghetti, M. Laser Ablation Synthesis in Solution and Size Manipulation of Noble Metal Nanoparticles. *Phys. Chem. Chem. Phys.* **2009**, *11*, 3805.
(7) Orozco-Montes, V.; Caillard, A.; Brault, P.; Chamorro-Coral, W.; Bigarre, J.; Sauldubois, A.; Andreazza, P.; Cuynet, S.; Baranton, S.; Coutanceau, C. Synthesis of Platinum Nanoparticles by Plasma Sputtering onto Glycerol: Effect of Argon Pressure on Their Physicochemical Properties. *J. Phys. Chem. C* **2021**, *125*, 3169−3179.
(8) Bastús, N. G.; Merkoçi, F.; Piella, J.; Puntes, V. Synthesis of Highly Monodisperse Citrate-Stabilized Silver Nanoparticles of up to 200 Nm: Kinetic Control and Catalytic Properties. *Chem. Mater.* **2014**, *26*, 2836−2846.
(9) Hussain, M. H.; Abu Bakar, N. F.; Mustapa, A. N.; Low, K.-F.; Othman, N. H.; Adam, F. Synthesis of Various Size Gold Nanoparticles by Chemical Reduction Method with Different Solvent Polarity. *Nanoscale Res. Lett.* **2020**, *15*, 140.
(10) Yang, M.; Zhu, H.; Zheng, Y.; Zhang, C.; Luo, G.; Xu, Q.; Li, Q.; Zhang, S.; Goto, T.; Tu, R. One-Step Chemical Vapor Deposition Fabrication of Ni@NiO@graphite Nanoparticles for the Oxygen Evolution Reaction of Water Splitting. *RSC Adv.* **2022**, *12*, 10496−10503.
(11) Granqvist, C. G. Size distributions for ultrafine metal particles. *J. Phys. Colloq.* **1977**, *38*, C2-147−C2-150.
(12) Kiss, L. B.; Söderlund, J.; Niklasson, G. A.; Granqvist, C. G. New Approach to the Origin of Lognormal Size Distributions of Nanoparticles. *Nanotechnology* **1999**, *10*, 25−28.
(13) Amendola, V.; Pilot, R.; Frasconi, M.; Maragò, O. M.; Iatì, M. A. Surface Plasmon Resonance in Gold Nanoparticles: A Review. *J. Phys.: Condens. Matter* **2017**, *29*, No. 203002.
(14) Kelly, K. L.; Coronado, E.; Zhao, L. L.; Schatz, G. C. The Optical Properties of Metal Nanoparticles: The Influence of Size, Shape, and Dielectric Environment. *J. Phys. Chem. B* **2003**, *107*, 668−677.
(15) Agrawal, A.; Cho, S. H.; Zandi, O.; Ghosh, S.; Johns, R. W.; Milliron, D. J. Localized Surface Plasmon Resonance in Semiconductor Nanocrystals. *Chem. Rev.* **2018**, *118*, 3121−3207.
(16) Maier, S. A. *Plasmonics: Fundamentals and Applications*; Springer: New York, NY, 2007.
(17) Barbir, R.; Pem, B.; Kalčec, N.; Kastner, S.; Podlesnaia, K.; Csáki, A.; Fritzsche, W.; Vinković Vrček, I. Application of Localized Surface Plasmon Resonance Spectroscopy to Investigate a Nano-Bio Interface. *Langmuir* **2021**, *37*, 1991−2000.
(18) Koushki, E.; Mowlavi, A. A.; Hoseini, S. T. Application of Localized Surface Plasmon Resonance of Conjugated Gold Nanoparticles in Spectral Diagnosis of SARS-CoV-2: A Numerical Study. *Plasmonics* **2023**, *18*, 1847−1855.
(19) Wang, S.; Mamedova, N.; Kotov, N. A.; Chen, W.; Studer, J. Antigen/Antibody Immunocomplex from CdTe Nanoparticle Bioconjugates. *Nano Lett.* **2002**, *2*, 817−822.
(20) Edelstein, R. The BARC Biosensor Applied to the Detection of Biological Warfare Agents. *Biosens. Bioelectron.* **2000**, *14*, 805−813.
(21) Pantarotto, D.; Partidos, C. D.; Hoebeke, J.; Brown, F.; Kramer, E.; Briand, J.-P.; Muller, S.; Prato, M.; Bianco, A. Immunization with Peptide-Functionalized Carbon Nanotubes Enhances Virus-Specific Neutralizing Antibody Responses. *Chem. Biol.* **2003**, *10*, 961−966.
(22) Jamshed, A.; Iqbal, A.; Ali, S. A Quick Review on the Applications of Nanomaterials as Adsorbents. *MOJ Ecol. Environ. Sci.* **2023**, *8*, 86−89.
(23) Xiao, X.; Xu, Y.; Lv, X.; Xie, J.; Liu, J.; Yu, C. Electrochemical CO2 Reduction on Copper Nanoparticles-Dispersed Carbon Aerogels. *J. Colloid Interface Sci.* **2019**, *545*, 1−7.
(24) Herbaut, M.; Siaj, M.; Claverie, J. P. Nanomaterials-Based Water Splitting: How Far Are We from a Sustainable Solution? *ACS Appl. Nano Mater.* **2021**, *4*, 907−910.
(25) Mirnaziry, S. R.; Shameli, M. A.; Yousefi, L. Design and Analysis of Multi-Layer Silicon Nanoparticle Solar Cells. *Sci. Rep.* **2022**, *12*, No. 13259.
(26) Shilpa, G.; Kumar, P. M.; Kumar, D. K.; Deepthi, P. R.; Sadhu, V.; Sukhdev, A.; Kakarla, R. R. Recent Advances in the Development of High Efficiency Quantum Dot Sensitized Solar Cells (QDSSCs): A Review. *Mater. Sci. Energy Technol.* **2023**, *6*, 533−546.
(27) Ishida, T.; Murayama, T.; Taketoshi, A.; Haruta, M. Importance of Size and Contact Structure of Gold Nanoparticles for the Genesis of Unique Catalytic Processes. *Chem. Rev.* **2020**, *120*, 464−525.
(28) Hoshyar, N.; Gray, S.; Han, H.; Bao, G. The Effect of Nanoparticle Size on *in Vivo* Pharmacokinetics and Cellular Interaction. *Nanomedicine* **2016**, *11*, 673−692.
(29) Shinkai, M.; Yanase, M.; Honda, H.; Wakabayashi, T.; Yoshida, J.; Kobayashi, T. Intracellular Hyperthermia for Cancer Using Magnetite Cationic Liposomes: *In Vitro* Study. *Jpn. J. Cancer Res.* **1996**, *87*, 1179−1183.
(30) Chen, F.; Ehlerding, E. B.; Cai, W. Theranostic Nanoparticles. *J. Nucl. Med.* **2014**, *55*, 1919−1922.
(31) Mäki-Lohiluoma, E.; Säkkinen, N.; Palomäki, M.; Winberg, O.; Ta, H. X.; Heikkinen, T.; Kiljunen, E.; Kauppinen, A. Use of Machine Learning in Prediction of Granule Particle Size Distribution and Tablet Tensile Strength in Commercial Pharmaceutical Manufacturing. *Int. J. Pharm.* **2021**, *609*, No. 121146.
(32) Shin, C.; Choi, J.; Kwak, D.; Kim, J.; Yang, J.; Chae, S.; Kim, T. Evaluation of Size Distribution Measurement Methods for Sub-100 Nm Colloidal Silica Nanoparticles and Its Application to CMP Slurry. *ECS J. Solid State Sci. Technol.* **2019**, *8*, P3195−P3200.
(33) Merkus, H. G. *Particle Size Measurements: Fundamentals, Practice, Quality*; Particle Technology Series; Springer: New York, NY, 2009.
(34) Emil Kaya, E.; Kaya, O.; Alkan, G.; Gürmen, S.; Stopic, S.; Friedrich, B. New Proposal for Size and Size-Distribution Evaluation of Nanoparticles Synthesized via Ultrasonic Spray Pyrolysis Using Search Algorithm Based on Image-Processing Technique. *Materials* **2020**, *13*, 38.
(35) Klapetek, P.; Valtr, M.; Nečas, D.; Salyk, O.; Dzik, P. Atomic Force Microscopy Analysis of Nanoparticles in Non-Ideal Conditions. *Nanoscale Res. Lett.* **2011**, *6*, 514.
(36) Doak, J.; Gupta, R. K.; Manivannan, K.; Ghosh, K.; Kahol, P. K. Effect of Particle Size Distributions on Absorbance Spectra of Gold Nanoparticles. *Phys. E* **2010**, *42*, 1605−1609.
(37) Scotti, A.; Liu, W.; Hyatt, J. S.; Herman, E. S.; Choi, H. S.; Kim, J. W.; Lyon, L. A.; Gasser, U.; Fernandez-Nieves, A. The CONTIN Algorithm and Its Application to Determine the Size Distribution of Microgel Suspensions. *J. Chem. Phys.* **2015**, *142*, No. 234905.
(38) Jia, Z.; Li, J.; Gao, L.; Yang, D.; Kanaev, A. Dynamic Light Scattering: A Powerful Tool for In Situ Nanoparticle Sizing. *Colloids Interfaces* **2023**, *7*, 15.
(39) Glatter, O. A New Method for the Evaluation of Small-Angle Scattering Data. *J. Appl. Crystallogr.* **1977**, *10* (5), 415−421.
(40) Kestens, V.; Roebben, G.; Herrmann, J.; Jämting, Å.; Coleman, V.; Minelli, C.; Clifford, C.; De Temmerman, P.-J.; Mast, J.; Junjie, L.; et al. Challenges in the Size Analysis of a Silica Nanoparticle Mixture as Candidate Certified Reference Material. *J. Nanopart. Res.* **2016**, *18*, 171.
(41) Lee, H.; Kwak, D.-B.; Kim, S. C.; Pui, D. Y. H. Characterization of Colloidal Nanoparticles in Mixtures with Polydisperse and Multimodal Size Distributions Using a Particle Tracking Analysis and Electrospray-Scanning Mobility Particle Sizer. *Powder Technol.* **2019**, *355*, 18−25.
(42) Abbas, Z.; Holmberg, J. P.; Hellström, A. K.; Hagström, M.; Bergenholtz, J.; Hassellöv, M.; Ahlberg, E. Synthesis, Characterization

and Particle Size Distribution of TiO2 Colloidal Nanoparticles. *Colloids Surf., A* **2011**, *384*, 254−261.
(43) Varenne, F.; Devoille, L.; Makky, A.; Feltin, N.; Violleau, F.; Barratt, G.; Vauthier, C. Evaluation of the Size Distribution of a Multimodal Dispersion of Polymer Nanoparticles by Microscopy after Different Methods of Deposition. *J. Drug Delivery Sci. Technol.* **2020**, *60*, No. 102047.
(44) Mansour, Y.; Battie, Y.; En Naciri, A.; Chaoui, N. Determination of the Size Distribution of Metallic Colloids from Extinction Spectroscopy. *Nanomaterials* **2021**, *11*, 2872.
(45) Grand, J.; Auguié, B.; Le Ru, E. C. Combined Extinction and Absorption UV−visible Spectroscopy as a Method for Revealing Shape Imperfections of Metallic Nanoparticles. *Anal. Chem.* **2019**, *91*, 14639−14648.
(46) Battie, Y.; Resano-Garcia, A.; Chaoui, N.; Zhang, Y.; En Naciri, A. Extended Maxwell-Garnett-Mie Formulation Applied to Size Dispersion of Metallic Nanoparticles Embedded in Host Liquid Matrix. *J. Chem. Phys.* **2014**, *140*, No. 044705.
(47) Mo, J.; Zhang, Q.; Xia, P.; Chen, H.; Lu, Z.; Yang, H.; Chen, Y.; Xiao, W.; Wang, Y.; Liu, M. Another Method to Calculate Grain Size Distribution Parameters: Using Ising Model and Particle Swarm Optimization Algorithm. *Solid State Commun.* **2022**, *356*, No. 114961.
(48) Faílde, D.; Viqueira, J. D.; Mussa Juane, M.; Gómez, A. Using Differential Evolution to Avoid Local Minima in Variational Quantum Algorithms. *Sci. Rep.* **2023**, *13*, No. 16230.
(49) Tuersun, P.; Zhu, C.; Han, X.; Fang Ren, K.; Yin, Y. Light Extinction Spectrometry for Determining the Size Distribution and Concentration of Polydisperse Gold Nanospheres. *Optik* **2020**, *204*, No. 163676.
(50) Amendola, V.; Meneghetti, M. Size Evaluation of Gold Nanoparticles by UV−vis Spectroscopy. *J. Phys. Chem. C* **2009**, *113*, 4277−4285.
(51) Bastús, N. G.; Comenge, J.; Puntes, V. Kinetically Controlled Seeded Growth Synthesis of Citrate-Stabilized Gold Nanoparticles of up to 200 Nm: Size Focusing versus Ostwald Ripening. *Langmuir* **2011**, *27*, 11098−11105.
(52) Hendel, T.; Wuithschick, M.; Kettemann, F.; Birnbaum, A.; Rademann, K.; Polte, J. In Situ Determination of Colloidal Gold Concentrations with UV−vis Spectroscopy: Limitations and Perspectives. *Anal. Chem.* **2014**, *86*, 11115−11124.
(53) Pugliese, R.; Regondi, S.; Marini, R. Machine Learning-Based Approach: Global Trends, Research Directions, and Regulatory Standpoints. *Data Sci. Manage.* **2021**, *4*, 19−29.
(54) Janiesch, C.; Zschech, P.; Heinrich, K. Machine Learning and Deep Learning. *Electron. Mark.* **2021**, *31*, 685−695.
(55) Sarker, I. H. Machine Learning: Algorithms, Real-World Applications and Research Directions. *SN Comput. Sci.* **2021**, *2*, 160.
(56) Shiratori, K.; Bishop, L. D. C.; Ostovar, B.; Baiyasi, R.; Cai, Y.-Y.; Rossky, P. J.; Landes, C. F.; Link, S. Machine-Learned Decision Trees for Predicting Gold Nanorod Sizes from Spectra. *J. Phys. Chem. C* **2021**, *125*, 19353−19361.
(57) Tan, E. X.; Chen, Y.; Lee, Y. H.; Leong, Y. X.; Leong, S. X.; Stanley, C. V.; Pun, C. S.; Ling, X. Y. Incorporating Plasmonic Featurization with Machine Learning to Achieve Accurate and Bidirectional Prediction of Nanoparticle Size and Size Distribution. *Nanoscale Horiz.* **2022**, *7*, 626−633.
(58) Arzola-Flores, J. A.; González, A. L. Machine Learning for Predicting the Surface Plasmon Resonance of Perfect and Concave Gold Nanocubes. *J. Phys. Chem. C* **2020**, *124*, 25447−25454.
(59) Pinkus, A. Approximation Theory of the MLP Model in Neural Networks. *Acta Numer.* **1999**, *8*, 143−195.
(60) Emmert-Streib, F.; Yang, Z.; Feng, H.; Tripathi, S.; Dehmer, M. An Introductory Review of Deep Learning for Prediction Models With Big Data. *Front. Artif. Intell.* **2020**, *3*, 4.
(61) Moore, J. A.; Chow, J. C. L. Recent Progress and Applications of Gold Nanotechnology in Medical Biophysics Using Artificial Intelligence and Mathematical Modeling. *Nano Express* **2021**, *2* (2), No. 022001.
(62) Wei, J.; Chu, X.; Sun, X.; Xu, K.; Deng, H.; Chen, J.; Wei, Z.; Lei, M. Machine Learning in Materials Science. *InfoMat* **2019**, *1*, 338−358.
(63) Revignas, D.; Amendola, V. Artificial Neural Networks Applied to Colorimetric Nanosensors: An Undergraduate Experience Tailorable from Gold Nanoparticles Synthesis to Optical Spectroscopy and Machine Learning. *J. Chem. Educ.* **2022**, *99*, 2112−2120.
(64) Abbasi Moud, A. Recent Advances in Utility of Artificial Intelligence towards Multiscale Colloidal Based Materials Design. *Colloid Interface Sci. Commun.* **2022**, *47*, No. 100595.
(65) Tao, H.; Wu, T.; Aldeghi, M.; Wu, T. C.; Aspuru-Guzik, A.; Kumacheva, E. Nanoparticle Synthesis Assisted by Machine Learning. *Nat. Rev. Mater.* **2021**, *6*, 701−716.
(66) Schletz, D.; Breidung, M.; Fery, A. Validating and Utilizing Machine Learning Methods to Investigate the Impacts of Synthesis Parameters in Gold Nanoparticle Synthesis. *J. Phys. Chem. C* **2023**, *127*, 1117−1125.
(67) Ishimaru, A.; Kitamura, S.; Marks, R. J.; Tsang, L.; Lam, C. M.; Park, D. C. Particle-Size Distribution Determination Using Optical Sensing and Neural Networks. *Opt. Lett.* **1990**, *15*, 1221.
(68) Nascimento, C. A. O.; Guardani, R.; Giulietti, M. Use of Neural Networks in the Analysis of Particle Size Distributions by Laser Diffraction. *Powder Technol.* **1997**, *90*, 89−94.
(69) Guardani, R.; Nascimento, C. A. O.; Onimaru, R. S. Use of Neural Networks in the Analysis of Particle Size Distribution by Laser Diffraction: Tests with Different Particle Systems. *Powder Technol.* **2002**, *126*, 42−50.
(70) Deriemaeker, L.; Finsy, R. Shape and Size Determination by Laser Diffraction: Average Aspect Ratio and Size Distributions by Volume; Feasibility of Data Analysis by Neural Networks. *Part. Part. Syst. Charact.* **2005**, *22*, 5−13.
(71) Glaubitz, C.; Bazzoni, A.; Ackermann-Hirschi, L.; Baraldi, L.; Haeffner, M.; Fortunatus, R.; Rothen-Rutishauser, B.; Balog, S.; Petri-Fink, A. Leveraging Machine Learning for Size and Shape Analysis of Nanoparticles: A Shortcut to Electron Microscopy. *J. Phys. Chem. C* **2024**, *128*, 421−427.
(72) He, J.; He, C.; Zheng, C.; Wang, Q.; Ye, J. Plasmonic Nanoparticle Simulations and Inverse Design Using Machine Learning. *Nanoscale* **2019**, *11*, 17444−17459.
(73) Long, Y.; Ren, J.; Li, Y.; Chen, H. Inverse Design of Photonic Topological State via Machine Learning. *Appl. Phys. Lett.* **2019**, *114*, No. 181105.
(74) Liu, D.; Tan, Y.; Khoram, E.; Yu, Z. Training Deep Neural Networks for the Inverse Design of Nanophotonic Structures. *ACS Photonics* **2018**, *5*, 1365−1369.
(75) Xu, X.; Sun, C.; Li, Y.; Zhao, J.; Han, J.; Huang, W. An Improved Tandem Neural Network for the Inverse Design of Nanophotonics Devices. *Opt. Commun.* **2021**, *481*, No. 126513.
(76) Unni, R.; Yao, K.; Han, X.; Zhou, M.; Zheng, Y. A Mixture-Density-Based Tandem Optimization Network for on-Demand Inverse Design of Thin-Film High Reflectors. *Nanophotonics* **2021**, *10*, 4057−4065.
(77) *Handbook of Optical Constants of Solids*; Palik, E. D.; Ghosh, G., Eds.; Academic Press: San Diego, CA, 1998.
(78) Daimon, M.; Masumura, A. Measurement of the Refractive Index of Distilled Water from the Near-Infrared Region to the Ultraviolet Region. *Appl. Opt.* **2007**, *46*, 3811.
(79) Mackay, T. G.; Lakhtakia, A. The Transfer-Matrix Method in Electromagnetics and Optics. In *Synthesis Lectures on Electromagnetics*; Springer International Publishing: Cham, 2020. DOI: 10.1007/978-3-031-02022-3.
(80) Rumpf, R. C. Improved formulation of scattering matrices for semi-analytical methods that is consistent with convention. *Prog. Electromagn. Res. B* **2011**, *35*, 241−261.
(81) Werdehausen, D.; Staude, I.; Burger, S.; Petschulat, J.; Scharf, T.; Pertsch, T.; Decker, M. Design Rules for Customizable Optical Materials Based on Nanocomposites. *Opt. Mater. Express* **2018**, *8*, 3456.
(82) Basodi, S.; Ji, C.; Zhang, H.; Pan, Y. Gradient Amplification: An Efficient Way to Train Deep Neural Networks. *Big Data Min. Anal.* **2020**, *3*, 196−207.

(83) List of Deep Learning Layers—MATLAB & Simulink—MathWorks Nordic, 2024. https://se.mathworks.com/help/deeplearning/ug/list-of-deep-learning-layers.html.
(84) Yang, L.; Shami, A. On Hyperparameter Optimization of Machine Learning Algorithms: Theory and Practice. *Neurocomputing* **2020**, *415*, 295−316.
(85) DeCastro-García, N.; Muñoz Castañeda, Á. L.; Escudero García, D.; Carriegos, M. V. Effect of the Sampling of a Dataset in the Hyperparameter Optimization Phase over the Efficiency of a Machine Learning Algorithm. *Complexity* **2019**, *2019*, 1−16.
(86) Options for Training Deep Learning Neural Network—MATLAB Training Options—MathWorks Nordic, 2024. https://se.mathworks.com/help/deeplearning/ref/trainingoptions.html.
(87) Teulon, J.-M.; Godon, C.; Chantalat, L.; Moriscot, C.; Cambedouzou, J.; Odorico, M.; Ravaux, J.; Podor, R.; Gerdil, A.; Habert, A.; et al. On the Operational Aspects of Measuring Nanoparticle Sizes. *Nanomaterials* **2019**, *9*, 18.
(88) Wu, K.-J.; Torrente-Murciano, L. Continuous Synthesis of Tuneable Sized Silver Nanoparticles *via* a Tandem Seed-Mediated Method in Coiled Flow Inverter Reactors. *React. Chem. Eng.* **2018**, *3*, 267−276.
(89) Togashi, T.; Tsuchida, K.; Soma, S.; Nozawa, R.; Matsui, J.; Kanaizuka, K.; Kurihara, M. Size-Tunable Continuous-Seed-Mediated Growth of Silver Nanoparticles in Alkylamine Mixture via the Stepwise Thermal Decomposition of Silver Oxalate. *Chem. Mater.* **2020**, *32*, 9363−9370.
(90) Zong, R.; Wang, X.; Shi, S.; Zhu, Y. Kinetically Controlled Seed-Mediated Growth of Narrow Dispersed Silver Nanoparticles up to 120 Nm: Secondary Nucleation, Size Focusing, and Ostwald Ripening. *Phys. Chem. Chem. Phys.* **2014**, *16*, 4236.
(91) Pyatenko, A.; Yamaguchi, M.; Suzuki, M. Synthesis of Spherical Silver Nanoparticles with Controllable Sizes in Aqueous Solutions. *J. Phys. Chem. C* **2007**, *111*, 7910−7917.
(92) Teranishi, T.; Eguchi, M.; Kanehara, M.; Gwo, S. Controlled Localized Surface Plasmon Resonance Wavelength for Conductive Nanoparticles over the Ultraviolet to Near-Infrared Region. *J. Mater. Chem.* **2011**, *21*, 10238.
(93) Rashidian Vaziri, M. R.; Omidvar, A.; Jaleh, B.; Partovi Shabestari, N. Investigating the Extrinsic Size Effect of Palladium and Gold Spherical Nanoparticles. *Opt. Mater.* **2017**, *64*, 413−420.
(94) Chakraborty, I.; Pradeep, T. Atomically Precise Clusters of Noble Metals: Emerging Link between Atoms and Nanoparticles. *Chem. Rev.* **2017**, *117*, 8208−8271.
(95) De Coene, Y.; Deschaume, O.; Jooken, S.; Seré, S.; Van Cleuvenbergen, S.; Bartic, C.; Verbiest, T.; Clays, K. Advent of Plasmonic Behavior: Dynamically Tracking the Formation of Gold Nanoparticles through Nonlinear Spectroscopy. *Chem. Mater.* **2020**, *32*, 7327−7337.
(96) Chen, X.; Liu, P.; Jensen, L. Atomistic Electrodynamics Simulations of Plasmonic Nanoparticles. *J. Phys. D: Appl. Phys.* **2019**, *52*, No. 363002.
(97) Von Delft, J.; Ralph, D. C. Spectroscopy of Discrete Energy Levels in Ultrasmall Metallic Grains. *Phys. Rep.* **2001**, *345*, 61−173.
(98) Raza, S.; Kadkhodazadeh, S.; Christensen, T.; Di Vece, M.; Wubs, M.; Mortensen, N. A.; Stenger, N. Multipole Plasmons and Their Disappearance in Few-Nanometre Silver Nanoparticles. *Nat. Commun.* **2015**, *6*, No. 8788.
(99) Shcherbakov, M. V.; Brebels, A.; Shcherbakova, N. L.; Tyukov, A. P.; Janovsky, T. A.; Kamaev, V. A. A Survey of Forecast Error Measures. *World Appl. Sci. J.* **2013**, *24*, 171−176.
(100) Meyer, F. Topographic Distance and Watershed Lines. *Signal Process.* **1994**, *38*, 113−125.
(101) Haiss, W.; Thanh, N. T. K.; Aveyard, J.; Fernig, D. G. Determination of Size and Concentration of Gold Nanoparticles from UV−vis Spectra. *Anal. Chem.* **2007**, *79*, 4215−4221.
(102) Petit, C.; Lixon, P.; Pileni, M. P. In Situ Synthesis of Silver Nanocluster in AOT Reverse Micelles. *J. Phys. Chem. A* **1993**, *97*, 12974−12983.
(103) Ershov, V.; Tarasova, N.; Ershov, B. Evolution of Electronic State and Properties of Silver Nanoparticles during Their Formation in Aqueous Solution. *Int. J. Mol. Sci.* **2021**, *22*, 10673.

https://doi.org/10.1021/acs.jpcc.4c02459
J. Phys. Chem. C 2024, 128, 9662−9675